Chapter 6:
Efficient Multigrid Computation of Steady Hypersonic Flows

B. Koren, P. W. Hemker
Center for Mathematics and Computer Science,
P.O. Box 4079, 1009 AB Amsterdam, The Netherlands

Note: This work was supported by the European Space Agency (ESA), through Avions Marcel Dassault - Bréguet Aviation (AMD-BA).

ABSTRACT

In steady hypersonic flow computations, Newton iteration as a local relaxation procedure and nonlinear multigrid iteration as an acceleration procedure may both easily fail. In the present chapter, some remedies are presented for overcoming these problems. The equations considered are the steady, two-dimensional Navier-Stokes equations. The equations are discretized by an upwind finite volume method.

Collective point Gauss-Seidel relaxation is applied as the standard smoothing technique. In hypersonics this technique easily diverges. First, collective line Gauss-Seidel relaxation is applied as an alternative smoothing technique. Though promising, it also fails in hypersonics. Next, collective point Gauss-Seidel relaxation is reconsidered and improved; a divergence monitor is introduced and in case of divergence a switch is made to a local explicit time stepping technique. Satisfactory single-grid convergence results are shown for the computation of a hypersonic reentry flow around a blunt forebody with canopy.

Unfortunately, with this improved smoothing technique, standard nonlinear multigrid iteration still fails in hypersonics. The robustness improvements made therefore to the standard nonlinear multigrid method are a local damping of the restricted defect, a global upwind prolongation of the correction and a global upwind restriction of the defect. Satisfactory multigrid convergence results are shown for the computation of a hypersonic launch and reentry flow around a blunt forebody with canopy. For the test cases considered, it appears that the improved multigrid method performs significantly better than a standard nonlinear multigrid method. For the test cases considered it appears that the most significant improvement comes from the upwind prolongation, rather than from the upwind restriction and the defect damping.

1. INTRODUCTION

1.1. Governing equations

The flow equations considered are the steady, two-dimensional (2D) Navier-Stokes equations

$$\frac{\partial}{\partial x}\begin{bmatrix}\rho u\\ \rho u^2+p\\ \rho uv\\ \rho u(e+\frac{p}{\rho})\end{bmatrix}+\frac{\partial}{\partial y}\begin{bmatrix}\rho v\\ \rho vu\\ \rho v^2+p\\ \rho v(e+\frac{p}{\rho})\end{bmatrix}-$$

$$\frac{1}{Re}\left[\frac{\partial}{\partial x}\begin{bmatrix}0\\ \tau_{xx}\\ \tau_{xy}\\ \tau_{xx}u+\tau_{xy}v+\dfrac{1}{\gamma-1}\dfrac{1}{Pr}\dfrac{\partial(c^2)}{\partial x}\end{bmatrix}+\frac{\partial}{\partial y}\begin{bmatrix}0\\ \tau_{xy}\\ \tau_{yy}\\ \tau_{xy}v+\tau_{yy}u+\dfrac{1}{\gamma-1}\dfrac{1}{Pr}\dfrac{\partial(c^2)}{\partial y}\end{bmatrix}\right]=0, \qquad (1a)$$

with

$$\tau_{xx}=\frac{4}{3}\frac{\partial u}{\partial x}-\frac{2}{3}\frac{\partial v}{\partial y},$$
$$\tau_{xy}=\frac{\partial u}{\partial y}+\frac{\partial v}{\partial x}, \qquad (1b)$$
$$\tau_{yy}=\frac{4}{3}\frac{\partial v}{\partial y}-\frac{2}{3}\frac{\partial u}{\partial x},$$

and with the total energy satisfying, assuming a perfect gas,

$$e=\frac{1}{\gamma-1}\frac{p}{\rho}+\frac{1}{2}(u^2+v^2). \qquad (1c)$$

For a detailed description of the various other quantities used, assumptions made and so on, we refer to any standard textbook. Suffice it to say here that these are the full, steady, 2D, compressible Navier-Stokes equations with as main assumptions made: zero bulk viscosity and constant diffusion coefficients. (So, the flow is assumed to be laminar and its diffusion coefficients are assumed to be temperature-independent.) For $1/Re=0$, diffusion has vanished and the remaining equations are the Euler equations.

So far, real gas effects are not taken into account. The specific heat ratio γ of the di-atomic gas considered is assumed to be constant and determined by fully excited translational and rotational energies only. (Though it could easily be replaced by a function ranging from zero up to the full equipartition value, the vibrational energy is assumed to be zero.)

1.2. Discretization method

For a description of the basic computational method which is taken as a point of departure, we refer to Hemker and Spekreijse [1,2,3] and Koren [4,5,6]. Here we give a concise overview of the main characteristics only. For both the Euler and Navier-Stokes equations, we have considered first- and higher-order accurate discretizations. Since in solving all types of equations our multigrid solution methods are applied to the first-order discretized equations only (higher-order discretized equations are solved in an outer, single-grid defect correction iteration), here we likewise limit the description of the discretization to the first-order accurate one only.

The Navier-Stokes equations are discretized in their integral form. The discrete system of equations is obtained by dividing the integration region Ω into quadrilateral finite volumes $\Omega_{i,j}$ and by requiring that the conservation laws, Equation (1a) in integral form, hold for each finite volume separately. At each volume wall, this discretization requires the evaluation of the convective flux vector and, additionally for Navier-Stokes, the diffusive flux vector.

For the evaluation of the convective flux vector we use an upwind approach, which follows the principle of Godunov [7]. For the solution of the resulting 1D Riemann problem, we prefer the approximate Riemann solver of Osher and Solomon [8] in the P-variant of Hemker and Spekreijse [1], this for reasons of both accuracy and efficiency (see Hemker and Spekreijse [1] and Koren [6]). The left and right states in the 1D Riemann problem (which determine the accuracy of the convective discretization) are simply taken equal to those in the corresponding adjacent volumes, leading to first-order convection accuracy.

For the evaluation of the diffusive flux vector, we use a central finite volume technique (see Koren [6]). This technique is second-order accurate, but given the first-order accurate upwind discretization of the convective terms, the overall accuracy remains first-order.

2. BASIC MULTIGRID SOLUTION METHOD

For the solution of the nonlinear system of first-order accurate discretized Navier-Stokes equations, in the basic method a standard nonlinear multigrid technique is applied, with collective symmetric point Gauss-Seidel relaxation as the smoother. The solution process is started by nested iteration. In the relaxation method exact Newton iteration is used for the collective update of the four state vector components in each finite volume. Nested grids are applied such that each finite volume on a coarse grid is the union of 2×2 volumes on the next finer grid. Let $\Omega_1,\ldots,\Omega_{l-1},\Omega_l,\Omega_{l+1},\ldots,\Omega_L$ be a sequence of such nested grids, with Ω_1 the coarsest and Ω_L the finest grid, and let $N_l(q_l)=r_l$ denote the nonlinear system of first-order discretized Navier-Stokes equations on Ω_l, with r_l a possibly non-zero right-hand side related to the multigrid iteration. Then a single nonlinear multigrid cycle and the nested iteration, as applied in the basic solution method, are defined in the following way.

2.1. Nonlinear multigrid iteration

- Apply on Ω_l n_{pre} pre-relaxation sweeps to $N_l(q_l)=r_l$.
- Compute the defect $d_l=N_l(q_l)-r_l$ and restrict it to Ω_{l-1}: $d_{l-1}=I_l^{l-1}d_l$, where I_l^{l-1} is a restriction operator for right-hand sides.
- Compute on the next coarser grid Ω_{l-1} the right-hand side $r_{l-1}=N_{l-1}(q_{l-1})-d_{l-1}$. For the initial estimate of q_{l-1}, we use the latest obtained q_{l-1}.
- Approximate the solution of $N_{l-1}(q_{l-1})=r_{l-1}$ by the application of n_σ nonlinear multigrid cycles. Denote the approximation obtained as $\tilde{q}_{l-1}$.
- Correct the current solution by $q_l=q_l+\tilde{I}_{l-1}^{l}(\tilde{q}_{l-1}-q_{l-1})$, where $\tilde{I}_{l-1}^{l}$ is a linear prolongation operator for solutions.
- Apply on Ω_l n_{post} post-relaxation sweeps to $N_l(q_l)=r_l$.

For $l=1$, the coarse grid correction is skipped of course. For the restriction operator I_l^{l-1} and the prolongation operator $\tilde{I}_{l-1}^{l}$ we take

$$(r_{l-1})_{i,j}=(I_l^{l-1}r_l)_{i,j}=(r_l)_{2i-1,2j-1}+(r_l)_{2i-1,2j}+(r_l)_{2i,2j-1}+(r_l)_{2i,2j}, \tag{2a}$$

$$(\tilde{I}_{l-1}^{l}q_{l-1})_{2i-1,2j-1}=(\tilde{I}_{l-1}^{l}q_{l-1})_{2i-1,2j}=(\tilde{I}_{l-1}^{l}q_{l-1})_{2i,2j-1}=(\tilde{I}_{l-1}^{l}q_{l-1})_{2i,2j}=(q_{l-1})_{i,j}. \tag{2b}$$

If not mentioned otherwise, for n_σ, n_{pre} and n_{post} we use in the basic multigrid method at each level l: $n_\sigma=1$ and $n_{\text{pre}}=n_{\text{post}}=1$; i.e. as nonlinear multigrid cycles we use V-cycles with a single pre- and post-relaxation sweep per level.

2.2. Nested iteration

- Choose a (possibly crude) initial estimate q_1.
- Improve q_1 by a single nonlinear multigrid cycle as just defined above.
- Prolongate the improved approximation q_1 to Ω_2, yielding an initial estimate for q_2.
- Improve q_2 by a single nonlinear multigrid cycle as defined above.
- Continue the previous process until an initial estimate for q_L has been obtained by prolongation of q_{L-1}.

The prolongation operator for obtaining the first approximation on each next finer grid may be the piecewise constant operator (2b) or - preferably - a more accurate operator (for instance a bilinear operator).

2.3. Numerical results

To give a quick impression of the performance of our basic multigrid method, both outside and inside the hypersonic flow regime, we consider the following Euler flows: (i) the NACA0012-airfoil at $M_\infty = 0.63$, $\alpha = 2°$ (smooth subsonic flow) and $M_\infty = 0.85$, $\alpha = 1°$ (non-smooth transonic flow), and (ii) a blunt forebody with canopy at $M_\infty = 8.15$, $\alpha = 30°$ (non-smooth hypersonic flow).

2.3.1. Subsonic and transonic airfoil flow. As finest finest-grid for the NACA0012-airfoil we consider the 128×32 O-type grid given in Figure 1. In all corresponding multigrid cases, as coarsest grid we consider the corresponding 8×2 O-type grid. (Hence for the 128×32-grid we have $L = 5$.)

For the present two airfoil flows the multigrid convergence histories are given in Figures 2a and 2b. In both graphs, the residual ratio along the vertical axis is the ratio $\Sigma_{k=1}^{4} |(N_L(q_L^n))_k| / \Sigma_{k=1}^{4} |(N_L(q_L^1))_k|$, $L = 3,4,5$ versus the number of cycles performed; (i) one *multigrid* cycle being a V-cycle with $n_{pre} = n_{post} = 1$, $\forall l$, and (ii) for Ω_5 only, one *single-grid* cycle being the equivalent number of finest-grid relaxation sweeps. $|(N_L(q_L^n))_k|$ denotes the summation - over all volumes at Ω_L - of the absolute values of the k-th component in the first-order Euler defects, with q_L^n denoting the solution at Ω_L after the n-th multi- or single-grid cycle. Considering the corresponding single-grid convergence histories, for both non-hypersonic cases, the effectiveness of the multigrid method appears to be good.

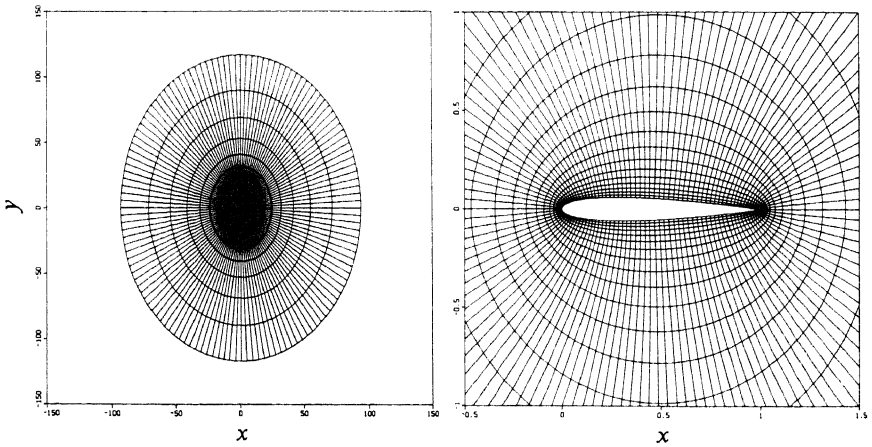

a. In full. b. In detail.

Figure 1. 128×32-grid (Ω_5) NACA0012-airfoil.

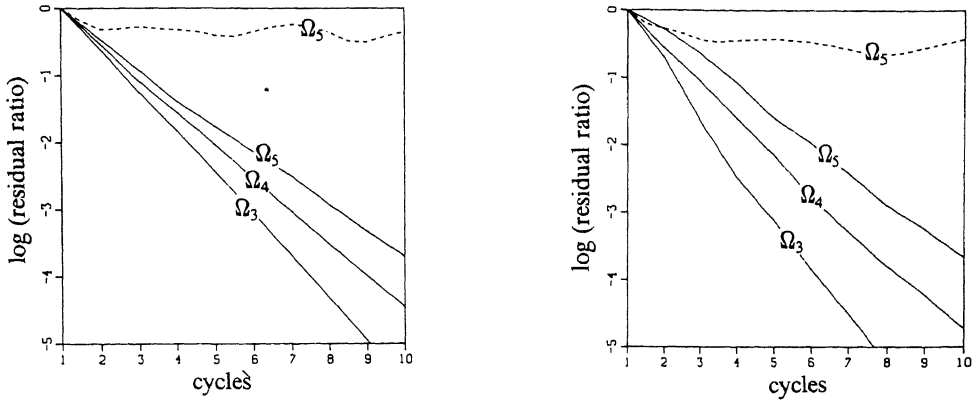

a. At $M_\infty = 0.63$, $\alpha = 2°$. b. At $M_\infty = 0.85$, $\alpha = 1°$.

Figure 2. Convergence histories NACA0012-airfoil at $1/Re = 0$
(------ : single-grid, —— : multigrid).

2.3.2. Hypersonic blunt body flow. However, for the hypersonic blunt body flow the results appear to be different. The forebody is composed out of two ellipse segments (Figure 3), given by

$$\left.\begin{aligned}\left(\frac{x}{0.06}\right)^2+\left(\frac{y}{0.015}\right)^2=1\\ \left(\frac{x}{0.035}\right)^2+\left(\frac{y}{0.025}\right)^2=1\end{aligned}\right\} \quad x<0, \tag{3a}$$

and a parallel part, given by

$$\left.\begin{aligned}y=-0.015\\ y=0.025\end{aligned}\right\} \quad 0\leqslant x\leqslant 0.016. \tag{3b}$$

As finest finest-grid, we consider here the 64×32 C-type grid given in Figure 4. As coarsest grid, the corresponding 4×2-grid is applied. (Hence, for this 64×32-grid we also have $L=5$.)

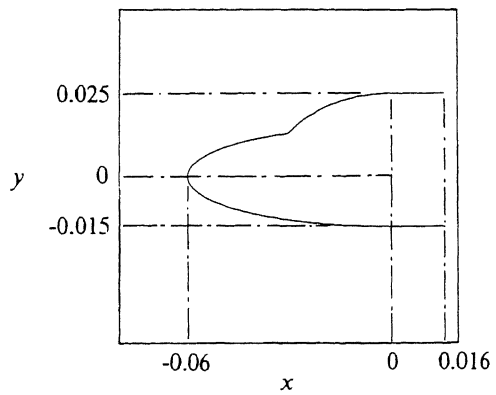

Figure 3. Blunt forebody with canopy.

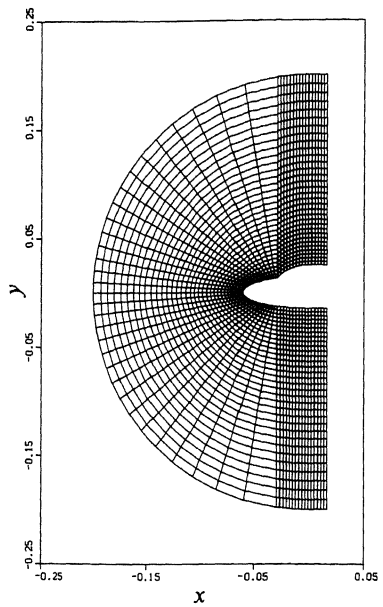

Figure 4. 64×32-grid (Ω_5) blunt forebody with canopy.

With this gridding, with the basic computational method described before and with an initial solution q_1 which is equal to the upstream far-field boundary conditions, *not any* flow solution could be obtained. Already in the first relaxation sweep on the coarsest grid, the solution process broke down! A new research topic was found: extension to hypersonics of the basic method's applicability.

3. IMPROVED MULTIGRID SOLUTION METHOD

It can be quickly understood that even single-grid, hypersonic blunt body flow computations may easily break down. In the initial phase of a steady flow computation in which strong solution perturbations arise, a local iterate may be easily swept out of the convergence range of the local Newton iteration and cause global divergence. (It is obvious that this may easily happen in the very first visit to the stagnation domain, during the computation of a hypersonic blunt body flow which has been - crudely - initialized to its hypersonic upstream flow conditions and in which a strong shock wave is arising.) Starting with a poor initial solution, one may gain in robustness by introducing a continuation process preceding the nested iteration. In such a process, usually a single upstream boundary condition, for instance M_∞, is increased from some low initial value to its correct high value, while performing relaxation sweeps. Continuation processes like this require a tuning of both the initial value and the increment. For hypersonic flow problems, proper tuning is difficult because of the fact that in these flows the condition numbers of the local derivative matrices used may be quite large. (The larger the condition numbers, the larger are the perturbations in the iterates induced by perturbations in the right-hand sides; right-hand side perturbations which may already be quite large by themselves in hypersonic flow computations.) The ill-conditioning occurring in hypersonic flow computations can be quickly illustrated for the 4×4 Eulerian derivative matrix $\nabla(\rho u, \rho u^2 + p, \rho uv, \rho u(e + p/\rho))$, where $\nabla \equiv (\partial/\partial u, \partial/\partial v, \partial/\partial c, \partial/\partial z)^T$, the differential operator applied in our solution method, and where $c \equiv \sqrt{\gamma p/\rho}$ and $z \equiv \ln(p\rho^{-\gamma})$. Considering for simplicity $v = 0$ and $p = 1$, it clearly appears from Figure 5 that the condition of $\nabla(\rho u, \rho u^2 + p, \rho uv, \rho u(e + p/\rho))$ becomes worse for $u/c \to \infty$. Notice further that the condition becomes worse also for $u/c \to 0$. The latter indi-

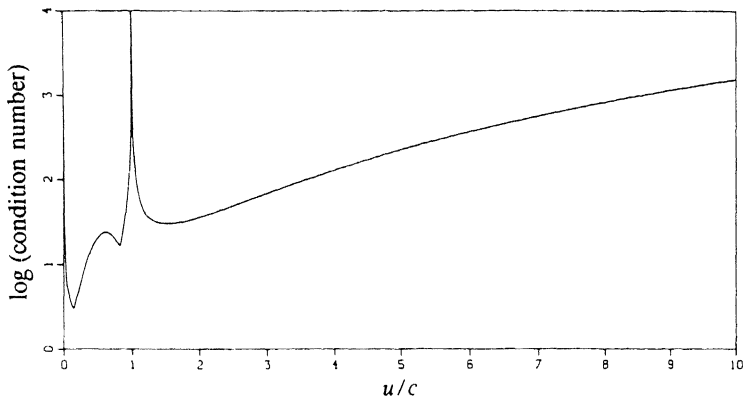

Figure 5. Condition of typical derivative matrix to be inverted, $v=0$, $p=1$, $1/Re=0$.

cates that stagnation flows become harder to relax with increasing upstream Mach number. (Further investigations for $1/Re \neq 0$ have shown us moreover that the poor performance of the point relaxation method is not restricted to inviscid stagnation flows, but also holds for the very low speed flows occurring in viscous sublayers.)

3.1. Line relaxation

If aforementioned situations are really of local nature, line relaxation may be a robust remedy. In a local, very low-subsonic flow region such as e.g. a viscous sublayer adjacent to the wall, relaxation lines crossing that layer and running into the outer solution (Figure 6a) are affected to a smaller extent by the low speeds than single volumes in that layer. For a strong hypersonic shock wave arising in an initially unperturbed flow field, a similar reasoning may hold for relaxation lines crossing that shock wave (Figure 6b) and single volumes in or downstream of that shock wave.

In a viscous sublayer with high aspect ratio volumes (such as in Figure 6a), an additional advantage of the properly directed line relaxation is that it is well-adapted to the corresponding strong coupling in crossflow direction. In convection dominated flow regions on the other hand, a strong coupling exists in flow direction. Here, relaxation lines are to be preferred which are more or less aligned with the flow. So, if well-aligned, this is an additional advantage of lines crossing shock waves.

With line Gauss-Seidel relaxation as an alternative smoother, the basic multigrid method may in principle be kept unchanged.

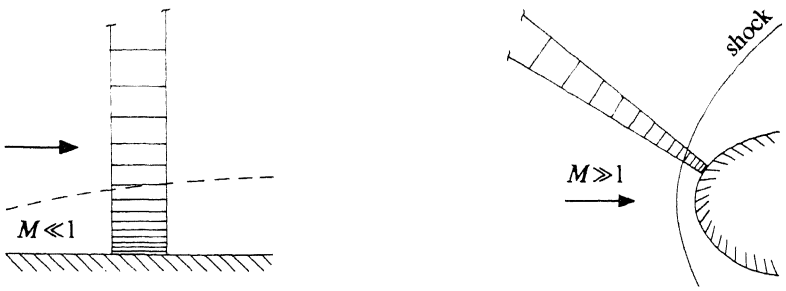

a. Viscous sublayer. b. Hypersonic shock wave.

Figure 6. Relaxation lines running out of difficult flow regions.

3.1.1. Relaxation matrix. For line relaxation applied in an Euler flow computation, two basic types of flows can be distinguished: flows with either (i) subsonic or (ii) supersonic velocity components along the relaxation line considered. For the subsonic case, the upwind discretization scheme (correctly) picks up its information from both upstream and downstream direction, with as a result: a block-tri-diagonal relaxation matrix. For the supersonic case the result is a block-bi-diagonal matrix. For Navier-Stokes flow computations a block-tri-diagonal matrix is the result in any case, except in the rare case of supersonic velocity components and zero gradients of u,v and c^2 along the relaxation line. (Then a block-bi-diagonal matrix results again.) In all cases the blocks are 4×4-matrices. In implementing the line relaxation, we did not put any special effort into an efficient solution of a block-bi- or -tri-diagonal system; a solver for a general band matrix is applied.

3.1.2. Numerical results for supersonic flat plate flow. As test case for studying the convergence of the multigrid method with line Gauss-Seidel relaxation as the new smoother, we start by considering a supersonic flat plate flow with an oblique shock wave impinging upon the plate (Euler) or upon the boundary layer (Navier-Stokes). The specific test case to be considered stems from Hakkinen et al. [9]. It is the experiment at $M_\infty=2$, $Re=2.96\ 10^5$. Since in this experiment, the flow is known to be laminar but yet hard to compute (because of the shock induced separation), it is a benchmark problem for laminar, 2D, compressible Navier-Stokes codes. A finest grid considered is the 80×32-grid shown in Figure 7. In all multigrid cases the coarsest grid considered is the corresponding 5×2-grid, hence for the grid in Figure 7 we have $L=5$. The grids have been optimized for convection by a stretching in flow direction and, in particular, by alignment with the impinging shock wave. A grid adaptation for diffusion has been realized by a stretching in crossflow direction. The initial solution is taken uniformly constant again and equal to the pre-shock inflow.

The convergence results are presented by the residual ratio $\Sigma_{k=1}^{4}|(N_L(q_L^n))_k|/\Sigma_{k=1}^{4}|(N_L(q_L^0))_k|$ versus either the amount of computational work (expressed in some appropriate work unit), or the (wall clock) time. In the residual ratio, N_L denotes again the discrete operator on the finest grid (either first-order Euler or first-order Navier-Stokes) and q_L^n the iterate after the n-th work unit, with q_L^0 the iterate obtained by the nested iteration. All these flat plate flow computations have been performed on a (two-pipe) Cyber 205.

For the *Euler* flow, the multigrid behaviors for Gauss-Seidel relaxation with successively points, crosswise lines and streamwise lines, are given in Figure 8. The streamwise line relaxation is symmetric whereas the other two relaxations are asymmetric with natural downwind sweeps only. To ensure a good comparison of the various convergence rates, we define a work unit to be equal to: a single multigrid cycle with symmetric relaxation, and consequently: two multigrid cycles with downwind relaxation only. Clearly visible in Figure 8 are the expected superior convergence rates and the better grid independence of the streamwise line relaxation.

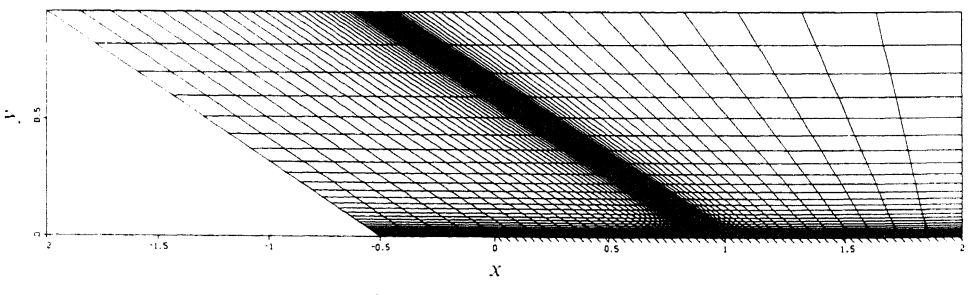

Figure 7. 80×32-grid (Ω_5) flat plate.

In Figure 9, still for the Euler equations, for three different finest grids, the multigrid efficiency with the streamwise line relaxation is compared with that with the point relaxation. The markers correspond with those in Figures 8a and 8c. Though no special effort was put into an efficient implementation of the line relaxation, it appears that its efficiency is the same for Ω_3 and better for Ω_4 and Ω_5. (The gain in efficiency on finer grids is of course a consequence of the better grid independence.)

Also for the *Navier-Stokes* situation ($Re = 2.96\ 10^5$), we consider the multigrid behaviors with point relaxation, crosswise line relaxation and streamwise line relaxation, successively. Here, all relaxations are symmetric, because of the occurrence of the subsonic sublayer. Further, the finest grid considered here is Ω_7 and a work unit is defined as one multigrid cycle with symmetric relaxation. The convergence rates are given in Figure 10. Both for point Gauss-Seidel relaxation and streamwise line Gauss-Seidel relaxation we have divergence at Ω_7. (For the latter relaxation we even have divergence at Ω_6.) In both relaxation cases the cause of divergence is the increasing ill-conditioning directly above the plate with decreasing mesh size normal to the plate. Here the crosswise line relaxation turns out to be robust.

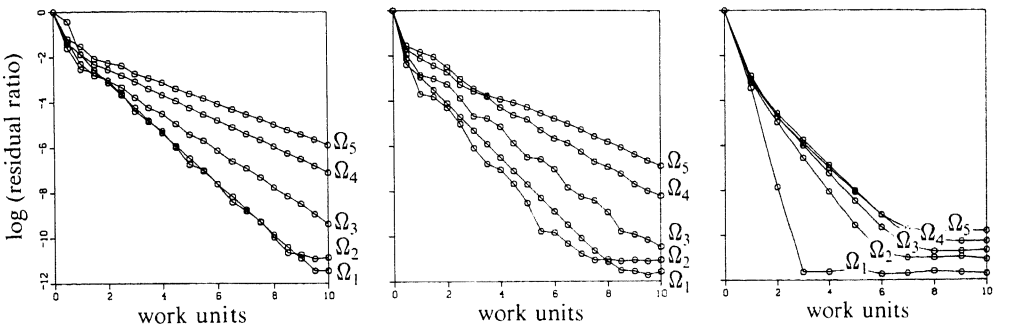

a. Point relaxation. b. Crosswise line relaxation. c. Streamwise line relaxation.

Figure 8. Multigrid convergence histories for three types of Gauss-Seidel relaxation, supersonic flat plate flow at $M_\infty = 2$, $1/Re = 0$.

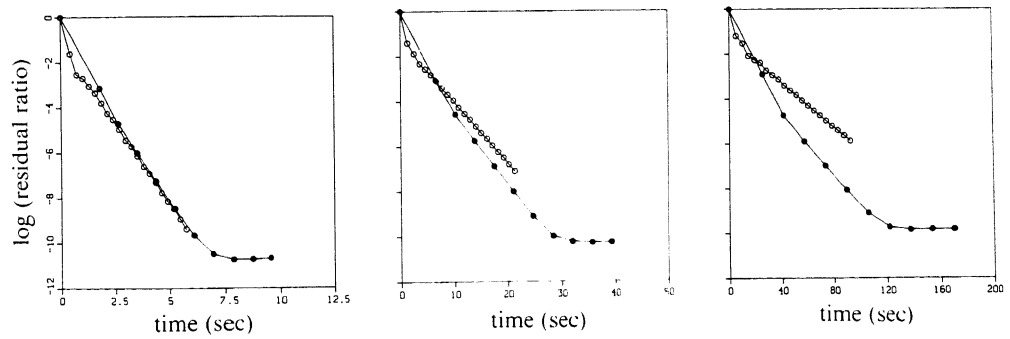

a. Ω_3. b. Ω_4. c. Ω_5.

Figure 9. Multigrid efficiencies for three finest grids, point (○) and streamwise line (●) Gauss-Seidel relaxation, supersonic flat plate flow at $M_\infty = 2$, $1/Re = 0$.

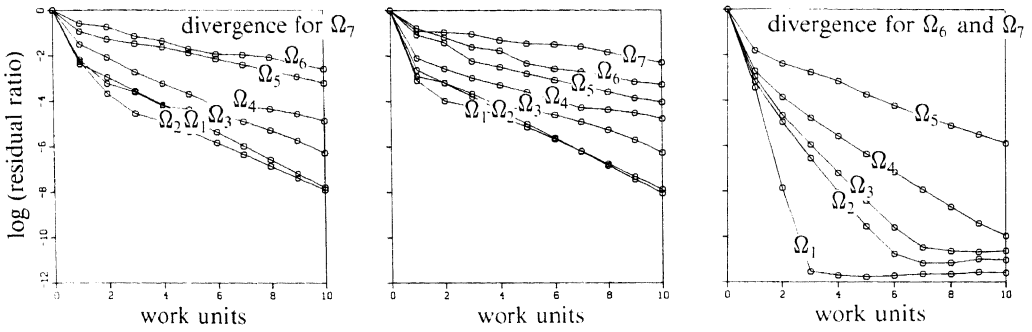

a. Point relaxation. b. Crosswise line relaxation. c. Streamwise line relaxation.

Figure 10. Multigrid convergence histories for three types of Gauss-Seidel relaxation, supersonic flat plate flow at $M_\infty = 2$, $Re = 2.96\ 10^5$.

An objection that can be made against the use of crosswise line relaxation throughout the computation is that though it is well-adapted to the strong coupling in the viscous sublayer with its high aspect ratio cells, it is not well-adapted to the opposite coupling in the outer flow. (There, streamwise lines are to be preferred.) The switch in direction of strong coupling suggests an adaptive local line relaxation to be optimal (Figure 11).

In conclusion: for the supersonic Euler flow considered, streamwise line relaxation appears to be most efficient. Already with a relatively slow solver for the large linear system, streamwise line relaxation may be more efficient than point relaxation. For Navier-Stokes flow computations with a practically relevant resolution of the viscous layers, crosswise line relaxation is to be preferred. Its advantage clearly is its greater robustness. It is less sensitive to a strong local ill-conditioning of the flow equations.

3.1.3. Numerical results for hypersonic blunt body flow. Unfortunately, for the hypersonic blunt body flow already considered in section 2.3.2, line Gauss-Seidel relaxation fails. In the next section we return to point Gauss-Seidel relaxation and introduce a robustness improvement for it: a switch to local, explicit time stepping.

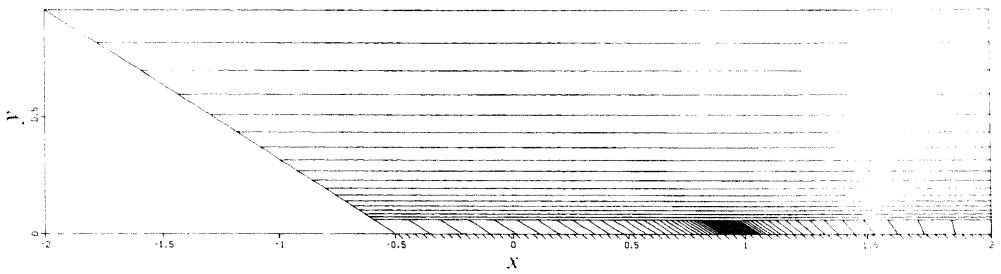

Figure 11. Locally adapted relaxation lines.

3.2. Switched-relaxation-evolution

In this section we do not yet consider the possibility of accelerating hypersonic flow computations by multigrid techniques. Here, we first restrict ourselves to the relaxation method only, particularly to its robustness. Further, we also restrict ourselves to the Euler equations ($1/Re = 0$).

As the remedy against failure of the Newton process in the point relaxation method, we use a switched-relaxation-evolution technique. In this technique, we simply start applying the basic, collective point Gauss-Seidel relaxation method and take measures only as soon as the local Newton iteration fails. To discuss these measures for robustness improvement, we consider the local, first-order discrete Euler system

$$\begin{aligned}\mathfrak{R}_{i,j}(q_{i,j}) \equiv\ & T^{-1}(\phi_{i+\frac{1}{2},j}) F(T(\phi_{i+\frac{1}{2},j}) q_{i,j}, T(\phi_{i+\frac{1}{2},j}) q_{i+1,j}) l_{i+\frac{1}{2},j} - \\ & T^{-1}(\phi_{i-\frac{1}{2},j}) F(T(\phi_{i-\frac{1}{2},j}) q_{i-1,j}, T(\phi_{i-\frac{1}{2},j}) q_{i,j}) l_{i-\frac{1}{2},j} + \\ & T^{-1}(\phi_{i,j+\frac{1}{2}}) F(T(\phi_{i,j+\frac{1}{2}}) q_{i,j}, T(\phi_{i,j+\frac{1}{2}}) q_{i,j+1}) l_{i,j+\frac{1}{2}} - \\ & T^{-1}(\phi_{i,j-\frac{1}{2}}) F(T(\phi_{i,j-\frac{1}{2}}) q_{i,j-1}, T(\phi_{i,j-\frac{1}{2}}) q_{i,j}) l_{i,j-\frac{1}{2}} = 0, \end{aligned} \tag{4}$$

where $T(\phi)$ denotes the matrix for rotation to a local coordinate system, $F(q^l, q^r)$ the numerical flux function (with its left and right cell face states q^l and q^r) and l the length of a finite volume wall. (For further details we refer to Hemker and Spekreijse [1].)

3.2.1. Failing Newton iteration. As a non-failing Newton iteration to solve $q_{i,j}$ from Equation (4) we define: a Newton iteration for which: (i)

$$\frac{|(\mathfrak{R}_{i,j}(q_{i,j}^{n+1}))_k|}{|(\mathfrak{R}_{i,j}(q_{i,j}^{n}))_k|} \leqslant 1, \quad k = 1,2,3,4, \quad \forall_{i,j}, \tag{5}$$

for any n-th Newton iterate ($n = 0,1,\ldots,N$) and each of the four residual components, and for which (ii) each iterate $q_{i,j}^{n+1}$ is physically correct, with physical correctness defined in the following way. Considering the local iterate $q_{i,j}^n = (u_{i,j}^n, v_{i,j}^n, c_{i,j}^n, z_{i,j}^n)^T$ and the corresponding hypersonic, upstream state vector $q_\infty = (u_\infty, v_\infty, c_\infty, z_\infty)^T$, we know that the flow speed may not exceed the value corresponding with adiabatic expansion to vacuum, starting from upstream conditions:

$$(u_{i,j}^n)^2 + (v_{i,j}^n)^2 \leqslant u_\infty^2 + v_\infty^2 + \frac{2}{\gamma - 1} c_\infty^2, \quad \forall_{i,j}. \tag{6}$$

Further, we know that after this expansion, the speed of sound equals zero, its minimally allowable value:

$$c_{i,j}^n \geqslant 0, \quad \forall_{i,j}. \tag{7}$$

The maximally allowable value of the speed of sound is that corresponding with the stagnation temperature (which is the same for both isentropic and non-isentropic compression). For adiabatic flows we can write:

$$c_{i,j}^n \leqslant \sqrt{c_\infty^2 + \frac{\gamma - 1}{2}(u_\infty^2 + v_\infty^2)}, \quad \forall_{i,j}. \tag{8}$$

For the lower limit of $z_{i,j}^n$ we can directly write with the entropy condition:

$$z_{i,j}^n \geqslant z_\infty, \quad \forall_{i,j}. \tag{9}$$

For the upper limit of $z_{i,j}^n$ we have to consider the state q_2 at the downstream side of a normal shock wave which has at its upstream side a state q_1 which has expanded to vacuum, departing from upstream conditions. Given the gas dynamics relations

$$p_2 = \frac{2\gamma M_1^2 - (\gamma - 1)}{\gamma + 1} p_1, \tag{10a}$$

$$\rho_2 = \frac{(\gamma + 1) M_1^2}{(\gamma - 1) M_1^2 + 2} \rho_1, \tag{10b}$$

$$p_1\rho_1^{-\gamma}=p_\infty\rho_\infty^{-\gamma}, \tag{10c}$$

it is clear that

$$z_{i,j}^n \leqslant \lim_{M_1\to\infty}\ln(p_2\rho_2^{-\gamma})=\infty, \quad \forall_{i,j}. \tag{11}$$

Summarizing, we see that in adiabatic flows both the flow speed and the speed of sound have a physical lower and upper limit. The entropy only has a lower limit.

In the algorithm, the relations (5)-(9) are checked after each update in each local Newton iteration. As soon as one or more of these five requirements are not satisfied, that local Newton iteration is said to have failed and the corresponding local correction found is rejected.

3.2.2. Evolution technique. As the alternative for a failing Newton iteration, we apply next one or eventually two explicit time stepping schemes to the local, semi-discrete system

$$\frac{\partial q_{i,j}}{\partial t}+\frac{1}{A_{i,j}}\mathfrak{F}_{i,j}(q_{i,j})=0. \tag{12}$$

with for $q_{i,j}$ here the conservative state vector $(\rho_{i,j},(\rho u)_{i,j},(\rho v)_{i,j},(\rho e)_{i,j})^T$ and for $A_{i,j}$ the area of finite volume $\Omega_{i,j}$.

As time stepping scheme to be applied first, we take the following version of the explicit, two-step rational Runge-Kutta scheme of Wambecq [10]:

$$q_{i,j}^{n+1}=q_{i,j}^n-\omega\frac{\tau_{i,j}^n}{A_{i,j}}\frac{\mathfrak{F}_{i,j}^2(q_{i,j}^n)}{2\mathfrak{F}_{i,j}(q_{i,j}^n)-\mathfrak{F}_{i,j}(q_{i,j}^n-\tfrac{1}{2}\omega\tau_{i,j}^n/A_{i,j}\mathfrak{F}_{i,j}(q_{i,j}^n))}, \quad n=0,1,\ldots,N, \tag{13}$$

with ω a possible damping factor for which we initially take $\omega=1$, and with $\tau_{i,j}^n$ the local time step for which we safely take the one which is maximally allowed for the forward Euler scheme:

$$\tau_{i,j}^n=\frac{A_{i,j}h_{i,j}}{\sup\left|\dfrac{d\mathfrak{F}_{i,j}(q_{i,j}^n)}{dq_{i,j}}\right|}, \tag{14}$$

with $h_{i,j}$ a characteristic local mesh size. With our upwind discretization, Equation (14) may be rewritten by good approximation as

$$\tau_{i,j}^n=\frac{h_{i,j}}{\sqrt{(u_{i,j}^n)^2+(v_{i,j}^n)^2}+c_{i,j}^n}. \tag{15}$$

For the evaluation of the denominator in scheme (13) we use the Samelson inverse of a vector:

$$\mathfrak{S}^{-1}\equiv|\mathfrak{S}|^{-2}\mathfrak{S}, \tag{16}$$

$\mathfrak{S}$ being a vector, whereas for the norm of a vector, we simply use the Cartesian inner product. As initial solution we take the same $q_{i,j}^0$ that just failed for the Newton iteration. The motivation for applying this scheme is its good stability as demonstrated in Wambecq [10] for a stiff and coupled system of four equations, which is precisely what we have here in hypersonics. However, a potential danger of scheme (13) is that there is no guarantee for the denominator to be non-zero.

To protect Wambecq's scheme against a possibly too large time step and against a (nearly) zero denominator, in each time step we require both the predictor and corrector to satisfy the conditions (6)-(9). As soon as a physically unrealistic value occurs, the time stepping is stopped immediately, rejecting any update made. Then, at first we assume that the unphysical result is due to a too large time step. Therefore, as a remedy, we take $\omega=\frac{1}{2}$ and restart the time stepping with Wambecq's scheme, using the same $q_{i,j}^0$. In case of re-occurrence of something unphysical, we assume that the denominator was the problem. Therefore, as a new remedy, we restart with an explicit time stepping scheme which is safe in this sense; the simple forward Euler scheme

$$q_{i,j}^{n+1} = q_{i,j}^{n} - \omega \frac{\tau_{i,j}^{n}}{A_{i,j}} \tilde{\mathfrak{N}}_{i,j}(q_{i,j}^{n}), \quad n = 0, 1, \ldots, N. \tag{17}$$

For $\tau_{i,j}^{n}$ in scheme (17) we also apply that according to relation (14). Further, for ω we continue with $\omega = \frac{1}{2}$ and for $q_{i,j}^{0}$ we also take the same as before. When a physically unrealistic value (according to the conditions (6)-(9)) occurs again, ω is halved for the second time and the time stepping with forward Euler is restarted, still using the same $q_{i,j}^{0}$. In case of something unphysical once more, the time stepping is stopped and the finite volume visited is left without any update being made. (Notice that for both time stepping schemes, we do not require condition (5) to be satisfied.)

With the present switched-relaxation-evolution approach we expect that in those volumes where Newton iteration fails, the local evolution technique will finally bring the solution into the attraction domain of the Newton iteration (for the next sweep) and so make itself quickly superfluous.

3.2.3. Numerical results for hypersonic blunt body flow. To illustrate the benefits of the switched-relaxation-evolution approach we consider again the hypersonic blunt body flow at $M_\infty = 8.15$, $\alpha = 30°$. In Figure 13, for the 16×8-, 32×16-, and 64×32-grids shown in Figure 12, we give the corresponding convergence behaviors obtained by the switched-relaxation-evolution technique. The residual ratio along the left vertical axes is again the ratio $\Sigma_{k=1}^{4} |(N_h(q_h^n))_k| / \Sigma_{k=1}^{4} |(N_h(q_h^0))_k|$. Here, the solution q_h^0 is the uniformly constant initial solution, which is equal to the hypersonic upstream boundary conditions. (Notice that these are single-grid results.) The quantity along the right vertical axes is the permillage of volumes in the total number of finite volumes visited during one cycle (one cycle being defined as two diagonally opposite, symmetric switched-relaxation-evolution sweeps), in which a switch to the evolution approach is made.

The robustness of the switched-relaxation-evolution technique is clear. For none of the cases considered is there an abortion of the solution process due to overflow or such. We even have convergence for all three cases. Further, from Figures 13b and 13c it appears that the evolution technique makes itself superfluous indeed in the course of the iteration process. The extension to Navier-Stokes can be quickly made. Only the time step needs to be reconsidered for diffusion. For this we refer to e.g. Hindmarsh et al. [11].

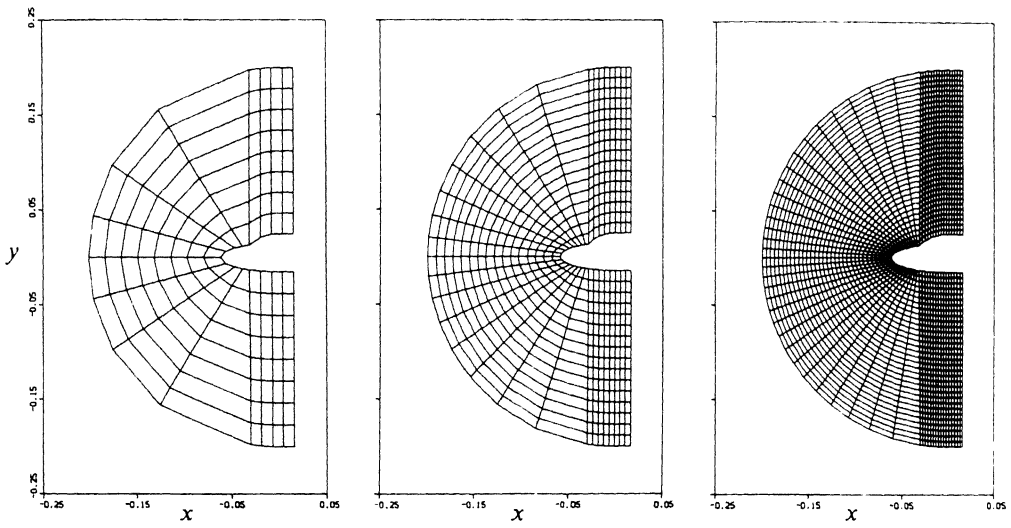

a. 16×8-grid. b. 32×16-grid. c. 64×32-grid.

Figure 12. Grids blunt forebody with canopy.

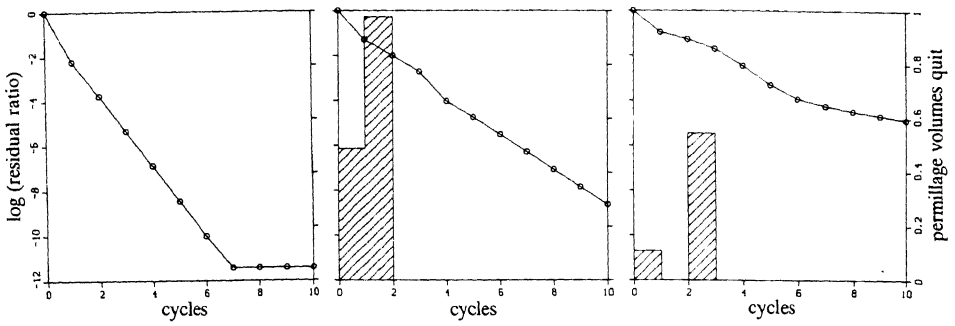

a. 16×8-grid. b. 32×16-grid. c. 64×32-grid.

Figure 13. Single-grid convergence results switched-relaxation-evolution technique, blunt forebody with canopy at $M_\infty = 8.15$, $\alpha = 30°$.

Notice that the convergence slow down with decreasing mesh size is expected for a plain relaxation method and is supposed to vanish by application of a suitable multigrid technique. Unfortunately, the switched-relaxation-evolution technique combined with the basic multigrid method as described in section 2, does not lead to satisfactory results; see Figure 14, with here for q_L^0 the approximate solution obtained by the nested iteration. Standard changes to the multigrid algorithm, such as for instance the replacement of V-cycles ($n_\sigma = 1$) by W-cycles ($n_\sigma = 2$) do not help. It appears that when applying multigrid to hypersonic test cases, in the standard way as described in section 2, local coarse-to-fine grid corrections may be transferred which sweep the corresponding fine grid iterates out of the attraction domain of the pure relaxation technique and even out of that of the switched-relaxation-evolution technique. The cause of these problems may be either the coarse grid corrections themselves, or the prolongation operator, or the combination of both. Therefore, in the next section, to avoid possibly bad coarse grid corrections, we present a local damping technique for the restricted defects and hence - implicitly - a local damping technique for the coarse grid corrections. To avoid a possibly bad correction transfer, in the next following section we also present an alternative prolongation: a direction-dependent prolongation. The improvements have already been published in Koren and Hemker [12]. For reasons of simplicity, here we keep ourselves restricted to the Euler equations.

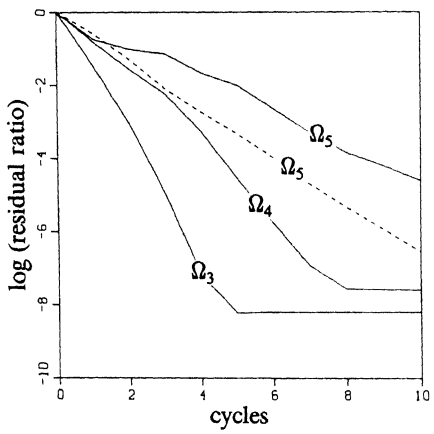

Figure 14. Convergence histories blunt forebody with canopy at $M_\infty = 8.15$, $\alpha = 0°$ (------ : single-grid, —— : multigrid).

However, in hypersonic flow computations, q_{l-1}^n and q_l^{n+1} may strongly differ from each other and as a consequence also both Jacobians in relation (23). For example, a hypersonic shock wave which is detached on Ω_l, may easily be attached on Ω_{l-1}, with as a probable consequence that there, locally relation (23) is not satisfied at all. If relation (23) is not satisfied, in particular if this is only very locally the case, damping of the restricted defect at those places might be useful. For optimal two-grid convergence, from Equation (22) we derive as local damping factor for the defect in finite volume $(\Omega_{l-1})_{i,j}$, to be applied in the $(n+1)$-st multigrid cycle:

$$(S_{l-1}^{n+1})_{i,j} = \min\left[1, \frac{\|(N'_{l-1})_{i,j}\|}{\max\left[\|(N'_l)_{2i-1,2j-1}\|, \|(N'_l)_{2i-1,2j}\|, \|(N'_l)_{2i,2j-1}\|, \|(N'_l)_{2i,2j}\|\right]}\right], \quad n=0,1,\ldots,N, \tag{25}$$

with $N'_{l-1} \equiv dN_{l-1}(q_{l-1}^n)/dq_{l-1}$, with $N'_l \equiv dN_l(q_l^{n+1})/dq_l$ and with $\|\cdot\|$ some matrix norm. Notice that the local damping factor (25) is more or less the 2D equivalent of the 1D damping introduced by De Zeeuw [13]. To see if some additional gain can be obtained by also allowing local defect amplification, in a numerical experiment we will also consider

$$(S_{l-1}^{n+1})_{i,j} = \frac{\|(N'_{l-1})_{i,j}\|}{\max\left[\|(N'_l)_{2i-1,2j-1}\|, \|(N'_l)_{2i-1,2j}\|, \|(N'_l)_{2i,2j-1}\|, \|(N'_l)_{2i,2j}\|\right]}, \quad n=0,1,\ldots,N. \tag{26}$$

At convergence of the solution, the defect multiplication will also have converged, both in case of multiplication (25) and in case of multiplication (26). However, as opposed to the correction damping proposed by Reusken [14], the present defect multiplication will probably not have vanished at convergence, neither in case of (25), nor in case of (26).

3.3.2. Numerical results for hypersonic blunt body flow. We proceed with evaluating the two defect multiplication techniques proposed. As the starting point for improvement we consider the multigrid results given in Figure 15. The results have been obtained for the blunt forebody with canopy at $M_\infty = 8.15$, $\alpha = 0°$, without any multigrid improvement and without nested iteration, but with the switched-relaxation-evolution approach. The initial solutions q_l^0, $l = 1,2,\ldots,L$ are taken uniformly constant and equal to the hypersonic upstream boundary conditions. In this way we obtain a poorer initial approximation, but we have a more discriminating test problem and we are ensured of an unambiguous evaluation, since q_l^0, $l = 1,2,\ldots,L$ will be the same for the different multigrid improvements to be considered.

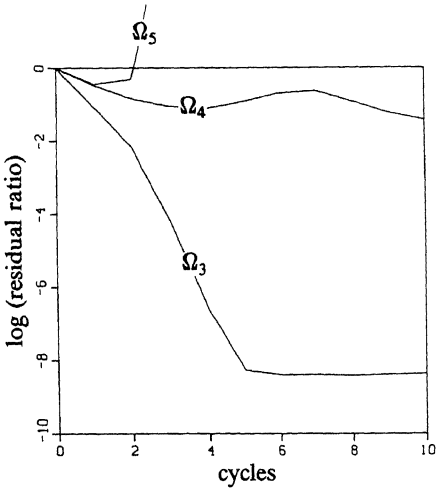

Figure 15. Multigrid convergence histories blunt forebody with canopy at $M_\infty = 8.15$, $\alpha = 0°$, without nested iteration and without any multigrid improvement.

With damping (25) as the defect multiplication, we obtain the convergence results given in Figure 16a. With the defect multiplication according to relation (26), both damping and amplification, we obtain the convergence results given in Figure 16b. For the matrix norms, in both relation (25) and relation (26), we applied the Frobenius-like norm

$$\|(N_l')_{2i,2j}\| = 2^l \left[\Sigma_{k_1=1,k_2=1}^{4,4} (N_l')^2_{k_1,k_2}\right]^{1/2}_{2i,2j}, \tag{27}$$

the factor 2^l simply accounting for the fact that in our case $N_l(q_l)$ is a line integral form. Corresponding with the results in Figures 16a and 16b, in Figures 17a and 17b we show distributions of the multiplication operator $S_{L-1}, L=5$ (the multiplication factor distribution on Ω_4), as applied in the last (i.e. the 10-th) multigrid cycle. In both cases the local damping is confined to only the close neighborhood of the blunt body. Locally, in Figure 17b the damping appears to be a little bit stronger than that in Figure 17a. However, globally this is more or less compensated by the local amplifications. Notice that the maximal amplification factor that was found to be applied in Figure 17b is still O(1) only. The minimal damping factors in Figures 17a and 17b are much larger than those found by De Zeeuw [13] for his specific nonlinear test case. A second difference is the good improvements found by De Zeeuw [13] for his basic multigrid method's performance and the present modest improvements. Both differences suggest that (at least) for the present test case, in order to significantly improve the results presented in Figure 15, defect multiplication is not needed as much as improved grid transfer operators; the topic of the next section.

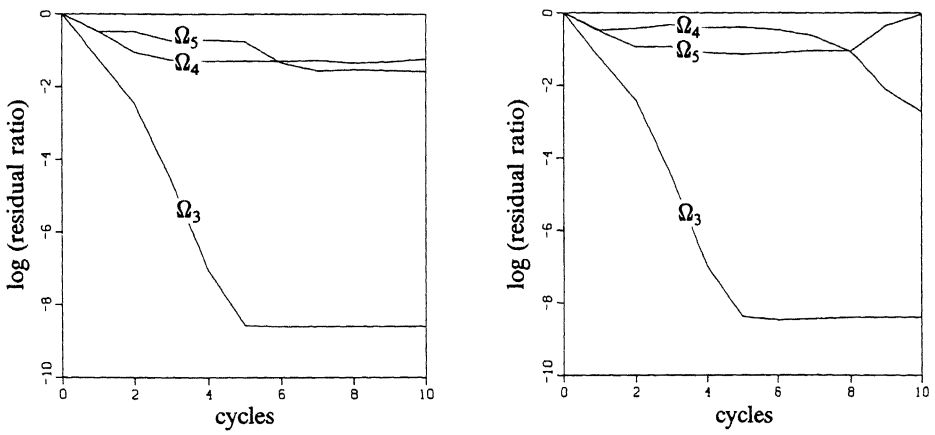

a. According to relation (25). b. According to relation (26).

Figure 16. Multigrid convergence histories blunt forebody with canopy at $M_\infty = 8.15$, $\alpha = 0°$, with defect multiplication.

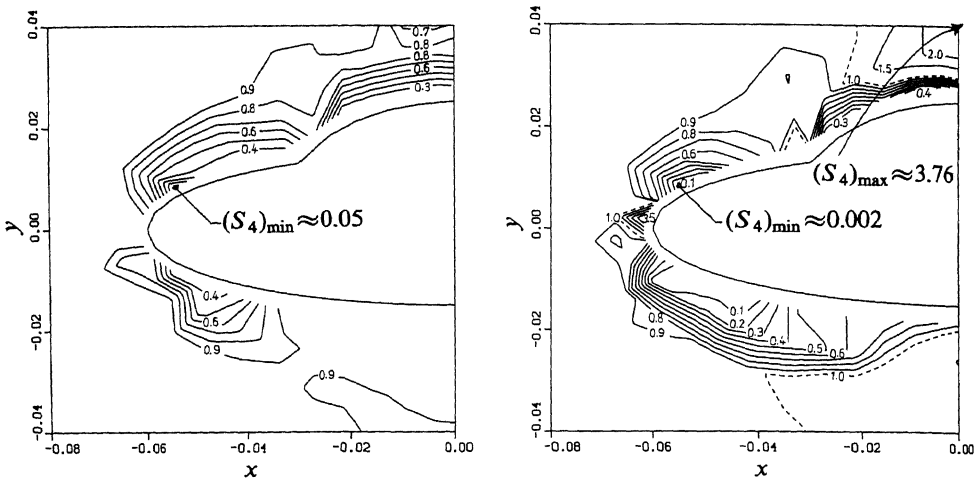

a. According to relation (25). b. According to relation (26).

Figure 17. Distribution multiplication factors applied on Ω_4 in the 10-th multigrid cycle, blunt forebody with canopy at $M_\infty = 8.15$, $\alpha = 0°$.

3.4. Direction-dependent grid transfer operators

3.4.1. Prolongation. The standard, piecewise constant correction prolongation may be illustrated as in Figure 18. In mathematical terms, solution correction by means of the piecewise constant correction prolongation may be written as

$$\begin{aligned}
(q_l^{new})_{2i-1,2j-1} &= (q_l^{old})_{2i-1,2j-1} + (\Delta q_{l-1})_{i,j}, \\
(q_l^{new})_{2i-1,2j} &= (q_l^{old})_{2i-1,2j} + (\Delta q_{l-1})_{i,j}, \\
(q_l^{new})_{2i,2j-1} &= (q_l^{old})_{2i,2j-1} + (\Delta q_{l-1})_{i,j}, \\
(q_l^{new})_{2i,2j} &= (q_l^{old})_{2i,2j} + (\Delta q_{l-1})_{i,j},
\end{aligned} \tag{28a}$$

with

$$(\Delta q_{l-1})_{i,j} = (q_{l-1}^{new})_{i,j} - (q_{l-1}^{old})_{i,j}. \tag{28b}$$

The direction-dependent correction prolongation that we propose now can be illustrated as in Figure 19. In mathematical terms - analogous to formulae (28) - solution correction by means of this direction-dependent prolongation is written as

$$\begin{aligned}
(q_l^{new})_{2i-1,2j-1} &= (q_l^{old})_{2i-1,2j-1} + \tfrac{1}{2}\left[(\Delta q_{l-1})_{i-1/2,j} + (\Delta q_{l-1})_{i,j-1/2}\right], \\
(q_l^{new})_{2i-1,2j} &= (q_l^{old})_{2i-1,2j} + \tfrac{1}{2}\left[(\Delta q_{l-1})_{i-1/2,j} + (\Delta q_{l-1})_{i,j+1/2}\right], \\
(q_l^{new})_{2i,2j-1} &= (q_l^{old})_{2i,2j-1} + \tfrac{1}{2}\left[(\Delta q_{l-1})_{i+1/2,j} + (\Delta q_{l-1})_{i,j-1/2}\right], \\
(q_l^{new})_{2i,2j} &= (q_l^{old})_{2i,2j} + \tfrac{1}{2}\left[(\Delta q_{l-1})_{i+1/2,j} + (\Delta q_{l-1})_{i,j+1/2}\right],
\end{aligned} \tag{29a}$$

with the four fine grid cell center corrections (Figure 19b) defined as *central* averages of the coarse grid cell face corrections (Figure 19a). The coarse grid cell face corrections are defined by

Given a left and right cell face state (q_{left} and q_{right}), for a general 1D upwind scheme, a cell face state q_{face} may be computed from

$$f(q_{\text{face}}) = F(q_{\text{left}}, q_{\text{right}}), \tag{30}$$

where $f(q)$ and $F(q_{\text{left}}, q_{\text{right}})$ denote the exact and numerical Euler flux function, respectively. A drawback of the Euler equations is that obtaining a primitive state vector like e.g. $q=(\rho,u,v,p)^T$ from $f(q)=(\rho u,\rho u^2+p,\rho uv,\rho u(e+p/\rho))^T$ requires the solution of a quadratic algebraic equation. Fortunately, with the P-variant of Osher's scheme (see Hemker and Spekreijse [1]), for most Riemann-problem cases arising in aeronautics $F(q_{\text{left}}, q_{\text{right}})=f(q_*)$, q_* being a well-defined, *single* state vector on the wave path connecting q_{left} and q_{right} in state space. Hence, with the P-variant, in most cases - without evaluating $F(q_{\text{left}}, q_{\text{right}})$ - we can directly identify q_{face} as $q_{\text{face}}=q_*$. For the O-variant of Osher's scheme (see Hemker and Spekreijse [1]), in almost all Riemann-problem cases arising in aeronautics $F(q_{\text{left}}, q_{\text{right}})$ is found to be the sum of three different fluxes $f(q)$. In these cases, because of $f(q)$'s nonlinearity, the previous simple procedure is not possible. In the (rare) cases where the P-variant also leads to a sum of fluxes, we solve the quadratic equation and in case of a positive discriminant and one zero being physically irrelevant (negative ρ and/or p), we take the zero which is physically relevant (positive ρ and p). In all other cases, we simply take $q_{\text{face}}=\frac{1}{2}(q_{\text{left}}+q_{\text{right}})$. Because of the consistency of Osher's scheme at boundaries, there the present upwind prolongation can also be applied in a consistent way. Notice that the upwind prolongation may lead to cell face states which are local extrema in state space. In conclusion, we emphasize that by replacing the piecewise constant prolongation operator by the present upwind prolongation operator, the complete numerical method has become more consistent. Both the discrete Euler operator and the correction prolongation operator are upwind now, both being based on the same upwind scheme: the P-variant of Osher's scheme.

3.4.2. Restriction. A provable consequence of the upwind prolongation is that no restriction operator I_l^{l-1} can be made for which the coarse grid finite volume discretization is a formal Galerkin approximation of the fine grid finite volume discretization. The possibly most effective restriction operator that can be really made is the exact adjoint of the nonlinear prolongation operator. Unfortunately - as opposed to the upwind prolongation - the exactly adjoint restriction operator will certainly lead to a significant increase of the computational overhead. More suitable seems to be a linear approximation of the exact (nonlinear) adjoint. For this we write the latest obtained coarse grid cell face states as linear combinations of the corresponding left and right states:

$$(q_{\text{face}})_k = a_k(q_{\text{left}})_k + (1-a_k)(q_{\text{right}})_k, \quad k=1,2,3,4, \tag{31a}$$

$$a_k = \frac{(q_{\text{face}})_k/(q_{\text{right}})_k - 1 + \epsilon/2}{(q_{\text{left}})_k/(q_{\text{right}})_k - 1 + \epsilon}, \quad \epsilon \ll 1, \tag{31b}$$

where q is the conservative state vector, $q=(\rho,\rho u,\rho v,\rho e)^T$, and ϵ a small parameter which guarantees that $(q_{\text{face}})_k$ is a central average in case $(q_{\text{left}})_k=(q_{\text{right}})_k=(q_{\text{face}})_k$. With next the central computation of the fine grid cell center states, we then have

$$\begin{aligned}(q_l)_{2i-1,2j-1,k} = (\tilde{I}_{l-1}^{l} q_{l-1})_{2i-1,2j-1,k} = {} & \tfrac{1}{2}(a_{l-1})_{i-\frac{1}{2},j,k}(q_{l-1})_{i-1,j,k} + \\ & \tfrac{1}{2}\left[2-(a_{l-1})_{i-\frac{1}{2},j,k}-(a_{l-1})_{i,j-\frac{1}{2},k}\right](q_{l-1})_{i,j,k} + \\ & \tfrac{1}{2}(a_{l-1})_{i,j-\frac{1}{2},k}(q_{l-1})_{i,j-1,k}, \quad k=1,2,3,4, \end{aligned} \tag{32a}$$

$$\begin{aligned}(q_l)_{2i-1,2j,k} = (\tilde{I}_{l-1}^{l} q_{l-1})_{2i-1,2j,k} = {} & \tfrac{1}{2}(a_{l-1})_{i-\frac{1}{2},j,k}(q_{l-1})_{i-1,j,k} + \\ & \tfrac{1}{2}\left[1-(a_{l-1})_{i-\frac{1}{2},j,k}+(a_{l-1})_{i,j+\frac{1}{2},k}\right](q_{l-1})_{i,j,k} + \\ & \tfrac{1}{2}\left[1-(a_{l-1})_{i,j+\frac{1}{2},k}\right](q_{l-1})_{i,j+1,k}, \quad k=1,2,3,4, \end{aligned} \tag{32b}$$

$$(q_l)_{2i,2j-1,k}=(\tilde{I}_{l-1}^{l}q_{l-1})_{2i,2j-1,k}=\tfrac{1}{2}\left[1-(a_{l-1})_{i+\frac{1}{2},j,k}\right](q_{l-1})_{i+1,j,k}+$$
$$\tfrac{1}{2}\left[1+(a_{l-1})_{i+\frac{1}{2},j,k}-(a_{l-1})_{i,j-\frac{1}{2},k}\right](q_{l-1})_{i,j,k}+$$
$$\tfrac{1}{2}(a_{l-1})_{i,j-\frac{1}{2},k}(q_{l-1})_{i,j-1,k},\quad k=1,2,3,4, \tag{32c}$$

$$(q_l)_{2i,2j,k}=(\tilde{I}_{l-1}^{l}q_{l-1})_{2i,2j,k}=\tfrac{1}{2}\left[1-(a_{l-1})_{i+\frac{1}{2},j,k}\right](q_{l-1})_{i+1,j,k}+$$
$$\tfrac{1}{2}\left[(a_{l-1})_{i+\frac{1}{2},j,k}+(a_{l-1})_{i,j+\frac{1}{2},k}\right](q_{l-1})_{i,j,k}+$$
$$\tfrac{1}{2}\left[1-(a_{l-1})_{i,j+\frac{1}{2},k}\right](q_{l-1})_{i,j+1,k},\quad k=1,2,3,4. \tag{32d}$$

With for q the conservative state vector $q=(\rho,\rho u,\rho v,\rho e)^T$, the linear relations (32a)-(32d) display how the upwind prolongation distributes mass, momentum and energy from a coarse grid to the overlying finer grid. For the approximately adjoint restriction operator (i.e. the approximation of the exact nonlinear adjoint), we can then write

$$(r_{l-1})_{i,j,k}=(I_l^{l-1}r_l)_{i,j,k}=\tfrac{1}{2}\left[1-(a_{l-1})_{i-\frac{1}{2},j,k}\right]\left[(r_l)_{2i-2,2j-1,k}+(r_l)_{2i-2,2j,k}\right]+$$
$$\tfrac{1}{2}\left[1-(a_{l-1})_{i,j-\frac{1}{2},k}\right]\left[(r_l)_{2i-1,2j-2,k}+(r_l)_{2i,2j-2,k}\right]+$$
$$\tfrac{1}{2}(a_{l-1})_{i+\frac{1}{2},j,k}\left[(r_l)_{2i+1,2j-1,k}+(r_l)_{2i+1,2j,k}\right]+$$
$$\tfrac{1}{2}(a_{l-1})_{i,j+\frac{1}{2},k}\left[(r_l)_{2i-1,2j+1,k}+(r_l)_{2i,2j+1,k}\right]+$$
$$\tfrac{1}{2}\left[2-(a_{l-1})_{i-\frac{1}{2},j,k}-(a_{l-1})_{i,j-\frac{1}{2},k}\right](r_l)_{2i-1,2j-1,k}+$$
$$\tfrac{1}{2}\left[1-(a_{l-1})_{i-\frac{1}{2},j,k}+(a_{l-1})_{i,j+\frac{1}{2},k}\right](r_l)_{2i-1,2j,k}+$$
$$\tfrac{1}{2}\left[1+(a_{l-1})_{i+\frac{1}{2},j,k}-(a_{l-1})_{i,j-\frac{1}{2},k}\right](r_l)_{2i,2j-1,k}+$$
$$\tfrac{1}{2}\left[(a_{l-1})_{i+\frac{1}{2},j,k}+(a_{l-1})_{i,j+\frac{1}{2},k}\right](r_l)_{2i,2j,k},\quad k=1,2,3,4. \tag{33}$$

Of course, the weak spot in the approach (31)-(32) is the linear approximation of the nonlinear prolongation. In case $(q_{\text{face}})_k$ is a local extremum, i.e. does not lie in between $(q_{\text{left}})_k$ and $(q_{\text{right}})_k$, we have a negative coefficient in relation (31a) (either a_k or $1-a_k$) and hence also in relation (33). We do not accept this situation. If occurring, locally and for that k-th component only, we neglect how the upwind prolongation really was and simply consider $(q_{\text{face}})_k=\tfrac{1}{2}((q_{\text{left}})_k+(q_{\text{right}})_k)$.

3.4.3. Numerical results for hypersonic blunt body flow. We now proceed with evaluating the direction-dependent grid transfer techniques. As starting point for improvement we consider again the multigrid results as obtained for the blunt forebody with canopy at $M_\infty=8.15$, $\alpha=0°$ without any multigrid improvement, but with the switched-relaxation-evolution approach. (See Figure 20, which is the same as Figure 15.) The multigrid behavior obtained after having replaced both the basic correction prolongation operator and the basic defect restriction operator by the direction-dependent operators, is given in Figure 21a. (We remark that defect damping is not applied.) With upwind grid transfers only, the improvement with respect to Figure 20 is significant indeed.

Replacing in the basic multigrid algorithm only the standard correction prolongation (by the upwind prolongation), we obtain the multigrid performance given in Figure 21b. These results are only a little bit less good than those in Figure 21a and hence make us conclude that the previous, rather cumbersome efforts in also upwinding the defect restriction, do not pay off enough. Therefore, in the following we refrain from applying the upwind restriction.

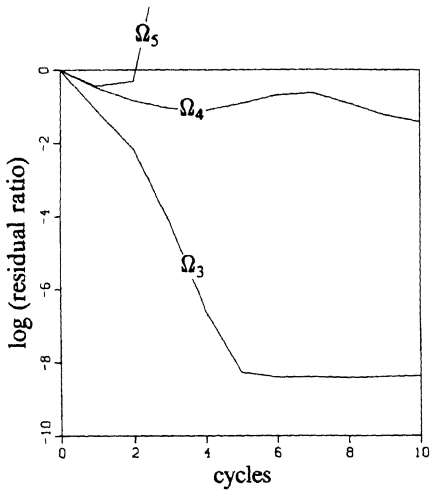

Figure 20. Multigrid convergence histories blunt forebody with canopy at $M_\infty = 8.15$, $\alpha = 0°$, without nested iteration and without any multigrid improvement.

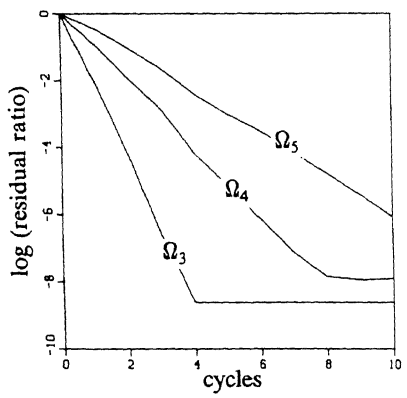

a. With upwind correction prolongation and upwind defect restriction.

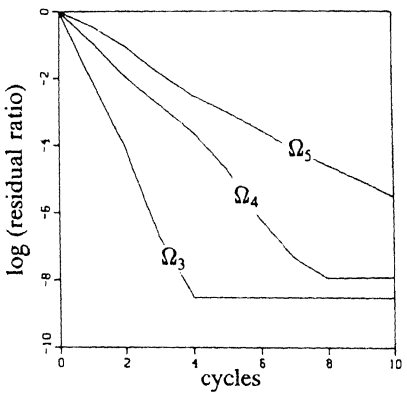

b. With upwind correction prolongation only.

Figure 21. Multigrid convergence histories blunt forebody with canopy at $M_\infty = 8.15$, $\alpha = 0°$.

3.5. Numerical results for hypersonic blunt body flow through combinations of multigrid improvements

3.5.1. Combination of defect damping and upwind correction prolongation. Though the two-grid convergence analysis in section 3.3.1 assumes that the prolongation operator is linear, see Equation (21), no reason exists why local defect multiplication would have a detrimental effect in combination with the nonlinear upwind prolongation. Therefore, in the present section, we show the multigrid performance for the combination of both defect damping and upwind correction prolongation. (Because the results in Figure 16b already showed not to be better than those in Figure 16a and because of the potential danger for divergence which is inherent to the allowance for local defect amplification, in the following - for the defect multiplication - we apply relation (25), i.e. damping, only.)

Combining both multigrid improvements as considered separately in sections 3.3 and 3.4, we obtain the results presented in Figure 22. Comparison with the results in Figure 21b learns that the combination of both techniques yields an only slightly better multigrid performance. We proceed with further investigating the combination. In Figure 23a we show the distribution of the operator $S_{L-1}, L=5$, as applied in the last (i.e. again the 10-th) multigrid cycle; a cycle in which the solution has already converged. First we notice that the damping has not vanished indeed. Further we notice that though the solution must be symmetrical around the front ellipse, the damping factor distribution is not. Cause of this is the fact that in the coarse grid problems, for the initial iterate, we take the latest iterate computed. (See the description of the nonlinear multigrid iteration in section 3.3.1: Equation (19).) By using the latest obtained iterate, the influence of the very first iterates is still felt, iterates which - due to their poor level of convergence - are not yet symmetrical around the front ellipse. An experimental proof of this explanation is given in Figure 23b in which we show the converged damping factor distribution for a strategy *with* solution restriction. Here, the converged damping factor distribution around the front ellipse is clearly symmetrical indeed. Notice that in both Figure 23a and Figure 23b the applied damping is modest. In Figure 23b - the case with solution restriction - it is even weaker than in Figure 23a. However, taking the restriction of the solution on the coarser grids usually leads to a slower convergence than taking the latest available coarse grid iterates.

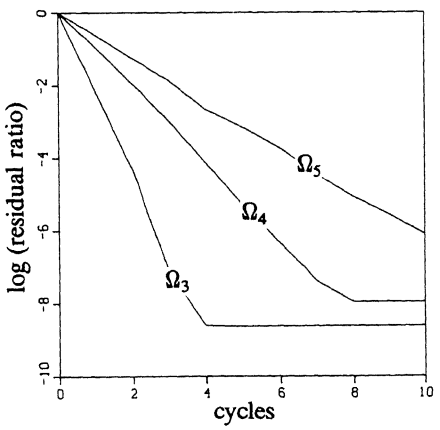

Figure 22. Multigrid convergence histories,
blunt forebody with canopy at $M_\infty = 8.15$, $\alpha = 0°$,
with both defect damping and upwind correction prolongation.

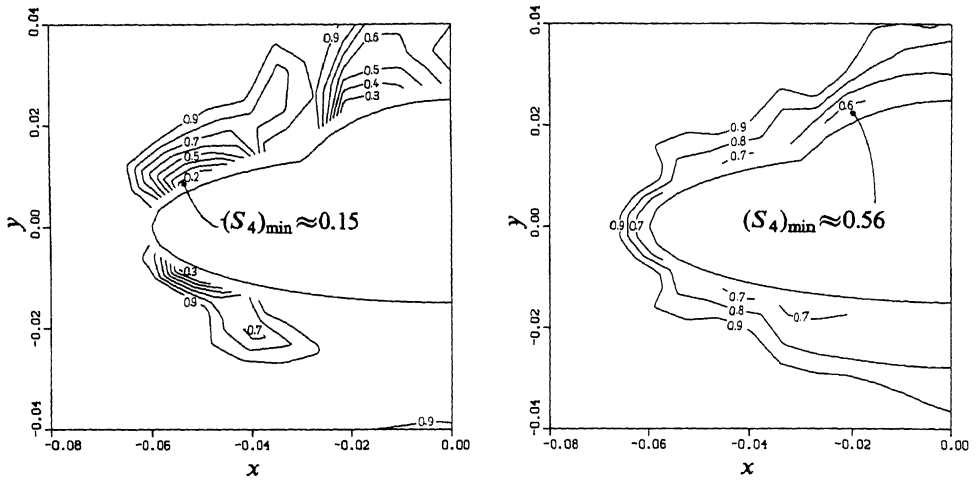

a. Without solution restriction.

b. With solution restriction.

Figure 23. Converged damping factor distributions on Ω_4, blunt forebody with canopy at $M_\infty = 8.15$, $\alpha = 0°$, with both defect damping and upwind correction prolongation.

3.5.2. Combination of defect damping, upwind correction prolongation and nested iteration. Comparing the basic multigrid method's results as presented in Figures 14 and 15 - results obtained *with* and *without* nested iteration, respectively - clearly shows the natural beneficial influence of nested iteration. For the improved multigrid method, the method with defect damping and upwind correction prolongation, the benefit of nested iteration (consistently, with upwind solution prolongation) is observed by counting the number of finite volumes in which - locally - the switch is made from the relaxation technique to the evolution technique (Figure 24). In both Figure 24a and Figure 24b (without and with nested iteration, respectively), the quantity along the vertical axis is a scaled number of switches made during the n-th multigrid cycle ($n = 1,2,...,10$), the scaling factor being the total number of volumes visited during one nonlinear multigrid cycle; a V-cycle with $n_{pre} = n_{post} = 1$ and with symmetric relaxation sweeps. (Notice that the scaling factor increases when going from Ω_3 to Ω_6.) The non-zero percentage at $n = 0$ in Figure 24b indicates the total amount of switches made during the nested iteration. For all four grids considered, the expected positive influence of the nested iteration appears to be significant.

In Figure 25 we give the multigrid convergence behavior corresponding with the latest favorite strategy, the strategy with defect damping, upwind prolongation and nested iteration. In this figure, for Ω_6, a comparison is also made with the corresponding single-grid convergence behavior. In Figure 26 we show the corresponding converged damping factor and Mach number distributions. Notice that the smallest damping factors are mainly concentrated along the bow shock, in particular there where the jumps across the shock are largest. Finally, we show results again for the more interesting reentry case $M_\infty = 8.15$, $\alpha = 30°$. Also for this test case, the convergence results (Figure 27) show the beneficial influence of the changes in the basic multigrid method. Given the very low convergence rate of the single-grid computation (Figure 27a) and given the absolute failure of the basic multigrid method (Figures 27a and 27b), the multigrid improvements do not just appear to be a nice luxury but a real necessity. Analogous to Figure 26, in Figure 28 we still show the converged damping factor and Mach number distributions. Notice that - like in Figure 26a - the smallest damping factors Figure 28a are located at the most pronounced part of the bow shock.

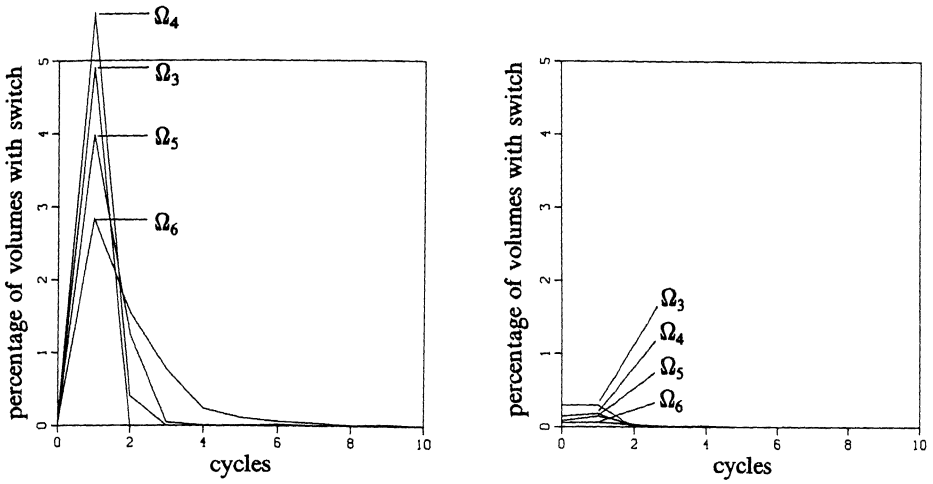

a. Without nested iteration.

b. With nested iteration.

Figure 24. Amount of volumes with switch from relaxation to evolution, percentage of volumes visited during one multigrid cycle, blunt forebody with canopy at $M_\infty = 8.15$, $\alpha = 0°$.

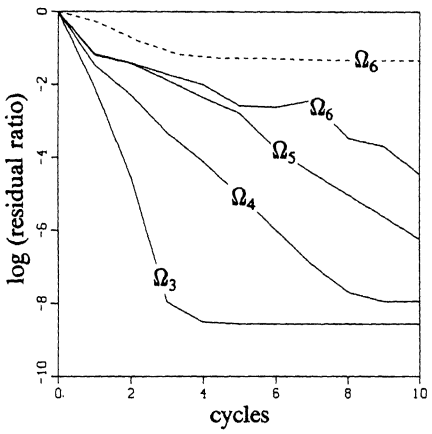

Figure 25. Convergence histories blunt forebody with canopy at $M_\infty = 8.15$, $\alpha = 0°$, with both defect damping, upwind prolongation and nested iteration, (------ : single-grid, —— : multigrid).

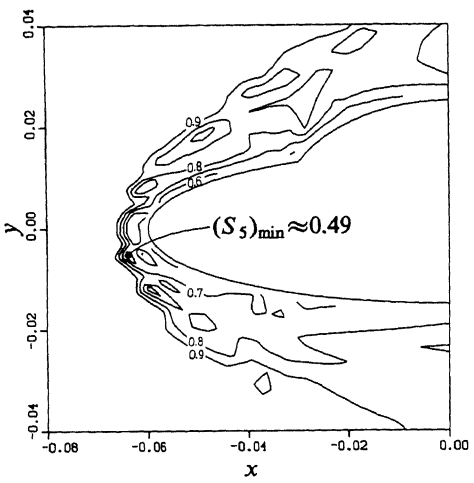

a. Damping factor distribution on Ω_5.

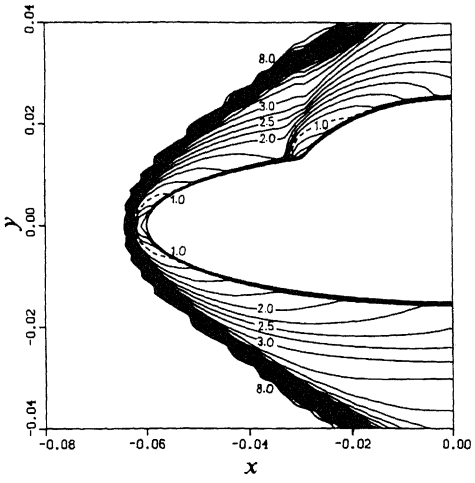

b. Mach number distribution on Ω_6.

Figure 26. Converged results blunt forebody with canopy at $M_\infty = 8.15$, $\alpha = 0°$, with both defect damping, upwind prolongation and nested iteration.

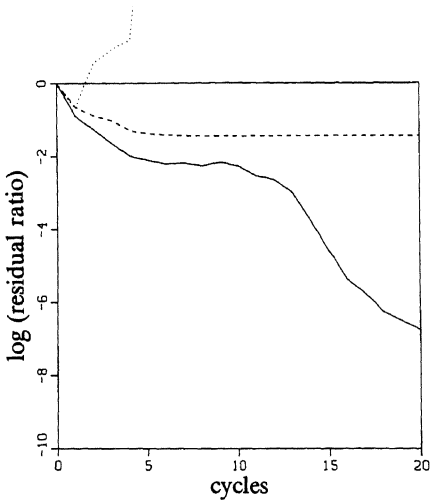

a. Convergence histories.

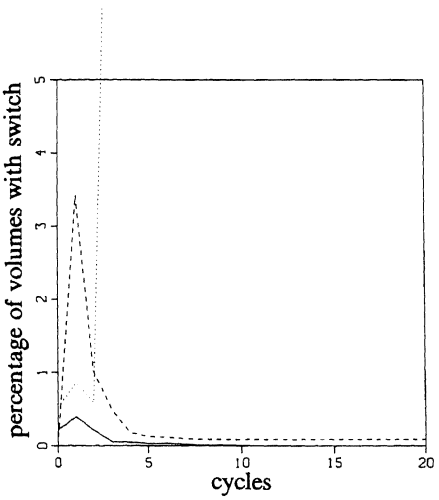

b. Amount of volumes with switch from relaxation to evolution, percentage of volumes visited during one multi-/single-grid cycle.

Figure 27. Iteration histories blunt forebody with canopy at $M_\infty = 8.15$, $\alpha = 30°$, with both defect damping, upwind prolongation and nested iteration, Ω_6 only, (------ : single-grid, ... : basic multigrid, —— : improved multigrid).

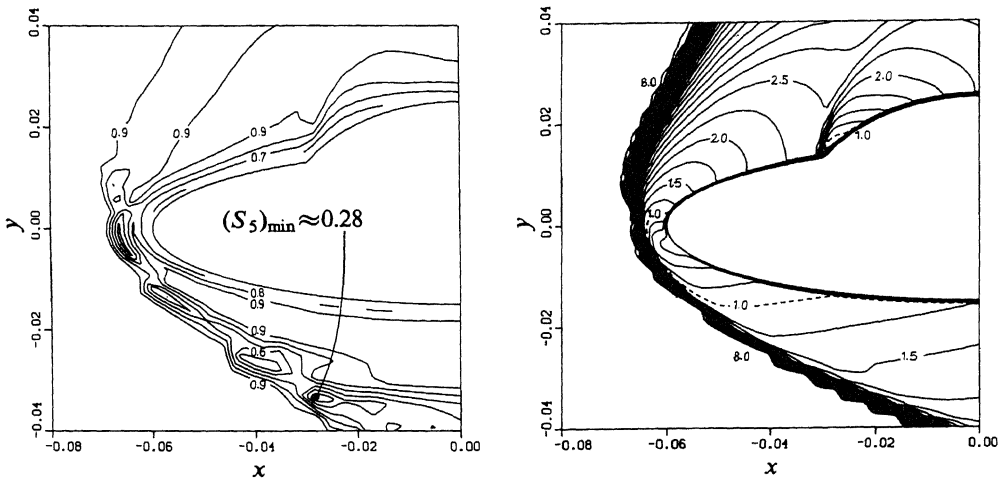

a. Damping factor distribution on Ω_5.

b. Mach number distribution on Ω_6.

Figure 28. Converged results blunt forebody with canopy at $M_\infty = 8.15$, $\alpha = 30°$, with both defect damping, upwind prolongation and nested iteration.

Concerning the efficiency of the improved multigrid method, one may find the paradoxical result that one multigrid cycle with both defect damping and upwind correction prolongation is still cheaper than one multigrid cycle without both. The cause of this simply is that the computations with the improved multigrid method may result in a significantly smaller number of switches from the local relaxation to a local evolution during the smoothing phases and hence in a lower computational cost. Concerning the efficiency of the upwind computation of cell face states (as applied in the upwind prolongation), for the test cases considered it appears that with the P-variant, at almost all cell faces it holds that $F(q_{left}, q_{right}) = f(q_*)$. (For both Ω_6-multigrid cases considered in this section, solving a quadratic equation for q_{face} appears to be necessary at about 1% of all cell faces only.)

To finish, we summarize the improved multigrid algorithm, the improvements being indicated in bold.

Nested iteration:
- Choose q_1.
- Improve q_1 by a single nonlinear multigrid cycle.
- Transfer the improved approximation q_1 to Ω_2, **by applying the upwind prolongation operator.**
- Improve q_2 by a single nonlinear multigrid cycle.
- Continue the previous process until an initial estimate for q_L has been obtained by **upwind prolongation** of q_{L-1}.

Nonlinear multigrid iteration:
- Apply n_{pre} pre-relaxation sweeps to $N_l(q_l)=r_l$.
- Compute the defect $d_l=N_l(q_l)-r_l$ and restrict it: $d_{l-1}=I_l^{l-1}d_l$.
- **Compute the local damping factors $(S_{l-1})_{i,j}$ and damp the restricted defect:** $d_{l-1}:=S_{l-1}d_{l-1}$.
- Compute the right-hand side $r_{l-1}=N_{l-1}(q_{l-1})-d_{l-1}$.
- Approximate the solution of $N_{l-1}(q_{l-1})=r_{l-1}$ by the application of n_σ nonlinear multigrid cycles.
- Correct the current solution, **by applying the upwind prolongation operator.**
- Apply n_{post} post-relaxation sweeps to $N_l(q_l)=r_l$.

4. CONCLUSIONS

For the hypersonic test cases considered in this paper, the essential element for robustness of the smoother is the continuous monitoring of both the local relaxation and the local evolution. The essential element for convergence appears to be the combination of Newton iteration, Wambecq's explicit, two-step rational Runge-Kutta scheme and the explicit Euler scheme. For steady Navier-Stokes flow computations at a finite Reynolds number, the proposed checks on physical correctness can be maintained as long as the flow remains adiabatic. Only the time step needs to be reconsidered for diffusion.

A satisfactory remedy against divergence of nonlinear multigrid appears to be the combination of a (local) damping of the restricted defect and a (global) upwind prolongation of the correction. Besides a positive influence on the robustness of the algorithm, the combination of upwind prolongation and defect damping also has a positive influence on the computational efficiency. Application - in addition - of an (approximately adjoint) upwind restriction operator does not really pay off. For the test cases considered, the best improvement is obtained by the application of the upwind prolongation operator. With this operator we have achieved a greater upwind consistency throughout the complete numerical method. For sake of clearness, we remark that the separate merits as observed here for the multigrid improvements, may well be different for other test cases. Just as for the switched-relaxation-evolution approach, the multigrid improvements are not restricted to the Euler equations, but can be carried over as well to the Navier-Stokes equations.

Finally, we remark that the new techniques are such that the improved algorithm, just like the basic algorithm, do not require any tuning of parameters.

REFERENCES

1. Hemker, P.W. and Spekreijse, S.P. Multiple Grid and Osher's Scheme for the Efficient Solution of the Steady Euler Equations, Applied Numerical Mathematics, Vol.2, pp. 475-493, 1986.

2. Hemker, P.W. Defect Correction and Higher Order Schemes for the Multi Grid Solution of the Steady Euler Equations, in Lecture Notes in Mathematics (Ed. Hackbusch, W. and Trottenberg, U.), Vol.1228, pp. 149-165, Proceedings of the Second European Conference on Multigrid Methods, Cologne, 1985. Springer-Verlag, Berlin and New York, 1986.

3. Spekreijse, S.P. Multigrid Solution of Monotone Second-Order Discretizations of Hyperbolic Conservation Laws, Mathematics of Computation, Vol.49, pp. 135-155, 1987.

4. Koren, B. Defect Correction and Multigrid for an Efficient and Accurate Computation of Airfoil Flows, Journal of Computational Physics, Vol.77, pp. 183-206, 1988.

5. Koren, B. Multigrid and Defect Correction for the Steady Navier-Stokes Equations, Journal of Computational Physics, Vol.87, pp. 25-46, 1990.

6. Koren, B. Upwind Discretization of the Steady Navier-Stokes Equations, International Journal for Numerical Methods in Fluids, Vol.11, pp. 99-117, 1990.

7. Godunov, S.K. Finite Difference Method for Numerical Computation of Discontinuous Solutions of the Equations of Fluid Dynamics (Cornell Aeronautical Lab. Transl. from the Russian), Matematicheskii Sbornik, Vol.47, pp. 271-306, 1959.

8. Osher, S. and Solomon, F. Upwind Difference Schemes for Hyperbolic Systems of Conservation Laws, Mathematics of Computation, Vol.38, pp. 339-374, 1982.

9. Hakkinen, R.J., Greber, I., Trilling, L. and Abarbanel, S.S. The Interaction of an Oblique Shock Wave with a Laminar Boundary Layer, Memo 2-18-59 W, NASA, Washington, 1959.

10. Wambecq, A. Rational Runge-Kutta Methods for Solving Systems of Ordinary Differential Equations, Computing, Vol.20, pp. 333-342, 1978.

11. Hindmarsh, A.C., Gresho, P.M. and Griffiths, D.F. The Stability of Explicit Euler Time-Integration for Certain Finite Difference Approximations of the Multi-Dimensional Advection-Diffusion Equation, International Journal for Numerical Methods in Fluids, Vol.4, pp. 853-897, 1984.

12. Koren, B. and Hemker, P.W. Damped, Direction-Dependent Multigrid for Hypersonic Flow Computations, Applied Numerical Mathematics, Vol.7, pp. 309-328, 1991.

13. De Zeeuw, P.M. Nonlinear Multigrid Applied to a One-Dimensional Stationary Semiconductor Model, SIAM Journal on Scientific and Statistical Computing (to appear).

14. Reusken, A.A. Convergence Analysis of Nonlinear Multigrid Methods, doctoral thesis, State University of Utrecht, Utrecht, 1988.